



HAL
open science

Anisotropic elastic properties of human cortical bone tissue inferred from inverse homogenization and resonant ultrasound spectroscopy

Xiran Cai, Laura Peralta, Renald Brenner, Gianluca Iori, Didier Cassereau,
Kay Raum, Pascal Laugier, Quentin Grimal

► To cite this version:

Xiran Cai, Laura Peralta, Renald Brenner, Gianluca Iori, Didier Cassereau, et al.. Anisotropic elastic properties of human cortical bone tissue inferred from inverse homogenization and resonant ultrasound spectroscopy. *Materialia*, 2020, 11, pp.100730. 10.1016/j.mtla.2020.100730 . hal-03212188

HAL Id: hal-03212188

<https://hal.science/hal-03212188v1>

Submitted on 29 Apr 2021

HAL is a multi-disciplinary open access archive for the deposit and dissemination of scientific research documents, whether they are published or not. The documents may come from teaching and research institutions in France or abroad, or from public or private research centers.

L'archive ouverte pluridisciplinaire **HAL**, est destinée au dépôt et à la diffusion de documents scientifiques de niveau recherche, publiés ou non, émanant des établissements d'enseignement et de recherche français ou étrangers, des laboratoires publics ou privés.

Anisotropic elastic properties of human cortical bone tissue inferred from inverse homogenization and resonant ultrasound spectroscopy

Xiran Cai^{a,*}, Laura Peralta^a, Renald Brenner^b, Gianluca Iori^c, Didier Cassereau^a, Kay Raum^c,
Pascal Laugier^a, Quentin Grimal^a

^aSorbonne Université, INSERM UMR-S 1146, CNRS UMR 7371, Laboratoire d'Imagerie Biomédicale, 75006 Paris, France

^bSorbonne Université, CNRS UMR 7190, Institut Jean le Rond d'Alembert, 75005 Paris, France

^cBerlin Brandenburg School of Regenerative Therapies, Charité-Universitätsmedizin Berlin, 13353 Berlin, Germany

Abstract

Bone extravascular matrix (EVM) elasticity at several tens micrometer scale plays a key role in the mechanical behavior of bone at different length scales with implications on bone biology through mechanotransduction. The elastic properties of cortical bone EVM have been evaluated by several experimental methods, including nanoindentation, scanning acoustic microscopy (SAM) and mechanical testing on μm sized bone specimens. Nevertheless, these methods hardly give access to elastic anisotropy. In this work, we propose a novel inverse homogenization method to evaluate the anisotropic elastic properties of cortical bone EVM based on the transverse isotropic elastic tensor of millimeter-sized bone specimens measured by using resonant ultrasound spectroscopy and Fast Fourier Transform homogenization method. With the inverse homogenization method, the anisotropic EVM stiffness constants were evaluated on 50 human femoral cortical bone specimens from an elderly group. To our knowledge, this is the first time that the whole set of the EVM stiffness tensor is evaluated on the same specimen and on a large number of samples. Further comparison with the results from SAM and the degree of mineralization of bone (DMB) showed the potential of this method. Empirical laws between DMB and EVM anisotropic stiffness constants were also provided for the first time. With the anisotropic elasticity evaluated by the proposed method, more accurate models can be developed to better understand bone mechanics and biology, such as mechanotransduction.

Keywords: Bone extravascular matrix, Anisotropic stiffness, Inverse homogenization, Resonant ultrasound spectroscopy

1. Introduction

Bone size, shape and chemical composition have evolved to reach a compromise between mass, resistance to fracture and amplitude of elastic deformations [1]. The elastic properties of bone tissue at the millimeter scale (or mesoscale) [2], which play a key role in bone mechanics, depend on the properties and organization of the constituents at the nanoscale (mineral crystals and collagen molecules), at the micrometer scale (aligned mineralized collagen fibers forming lamellae) [3], and at the scale of a few tenth of microns where osteons and vascular pores are the main microarchitectural features.

*Corresponding author

Email address: xirancai@stanford.edu (Xiran Cai)

18 Bone tissue at the micrometer scale, i.e., the solid material in which vessels and nerves are embedded
19 is often referred to as bone extravascular matrix (EVM), shortly bone matrix [4–6]. Bone material at
20 the mesoscale is accordingly modelled as a network of vascular canals (Haversian and Volkman canals)
21 embedded in a homogeneous bone matrix [7–9]. The elastic properties of EVM deserve a careful study
22 because, combined with the micro-architecture of the vascular porosity, they determine bone elasticity at
23 the mesoscale, which has a direct impact on the macroscopic mechanical behavior of whole bone. Also, for a
24 given macroscopic loading, bone matrix elastic properties play a role in mechanotransduction as they govern
25 the amplitude of matrix deformations which determine the interstitial fluid flow and the local strains sensed
26 by osteocytes [10].

27 While, the inter-individual variations of EVM elastic properties in the general population are expected to
28 be small [11, 12], considerable alteration of matrix elastic properties have been observed as a consequence of
29 bone pathologies [13–15] and drugs [16, 17]. Several experimental approaches have been proposed to measure
30 EVM elastic properties, which can be categorized as direct and indirect approaches. Direct approaches are
31 nanoindentation [18, 19], scanning acoustic microscopy (SAM) [11, 20] and mechanical testing on μm -sized
32 bone specimens [21–23]. For instance, using nano-indentation, elastic properties of trabecular and cortical
33 bone tissues were found to be similar [24] and the interstitial tissue was found to be stiffer than osteonal
34 tissue [25]. Using SAM, it was found that collagen fiber orientation has an impact on tissue elastic anisotropy
35 probed at the microscale [26, 27].

36 These direct approaches have several limitations. Several assumptions on tissue elasticity (isotropy, as-
37 sumed Poisson’s ratio) are necessary to obtain the Young’s modulus from a nanoindentation load-displacement
38 curve [28]. Also, to get a representative value of bone matrix elasticity, several tens of indentation locations
39 must be considered in the osteonal and interstitial tissues. SAM yields a map of the acoustic reflectivity of a
40 bone surface using a high frequency ultrasound probe. Precisely, the method yields acoustic impedance val-
41 ues which can only be converted to Young’s modulus using assumptions on tissue composition and Poisson’s
42 ratio [29]. Mechanical testing on μm -sized specimens requires dedicated experimental apparatus, long speci-
43 men’s preparation time and it is not always possible to achieve a testing environment mimicking physiological
44 conditions, e.g., as for experiments conducted in an electronic microscope [22].

45 An indirect approach to measure trabecular tissue elasticity was introduced by van Rietbergen et al. [30];
46 Tissue elasticity is retrieved by back-calculation combining experimental mechanical testing on a specimen
47 of several millimeters and a corresponding micro-finite element model accounting for the specimen-specific
48 trabecular microarchitecture. A linear relationship between tissue Young’s modulus and bulk (measured)
49 modulus can be assumed, which makes it possible to infer tissue modulus by searching for a good match
50 between model and experimental data. A similar approach was proposed in which mechanical testing was
51 replaced by ultrasound resonance testing [31].

52 Direct methods are designed to probe the EVM elastic modulus in one single direction (typically along the
53 osteon axis), and inverse methods, as used to retrieve matrix elasticity in trabecular bone, assume isotropic

54 properties. This is a major limitation of both direct and indirect approaches: they hardly give access to
 55 elastic anisotropy unless very specific and elaborated techniques are implemented [19, 32]. However, EVM
 56 is not isotropic [25, 33, 34].

57 The present article introduces a novel indirect approach to retrieve the anisotropic EVM elastic properties.
 58 The new method is applied to a collection of human specimens to document the EVM elastic properties in an
 59 elderly population. Our approach, coined inverse homogenization, is similar to the back calculation procedure
 60 introduced by van Rietbergen et al. [30] for trabecular bone but it uses anisotropic elastic information at the
 61 mesoscale (experimental data) and the computation of a specimen’s elastic tensor with homogenization. The
 62 method combines resonant ultrasound spectroscopy (RUS) which accurately measures the transverse isotropic
 63 elastic tensor of millimeter-sized bone specimens [35, 36] and Fast Fourier Transform (FFT) homogenization
 64 method [37, 38], which has been widely used in engineering material mechanics to evaluate the effective
 65 properties of composites and porous materials.

66 2. Materials and methods

67 2.1. Sample preparation

68 Bone specimens were harvested from the left femur of 29 human cadavers, provided by the Département
 69 Universitaire d’Anatomie Rockefeller (French body donation to science program, declaration number: DC-
 70 2015–2357; Laboratory of Anatomy, Faculty of Medicine Lyon Est, University of Lyon, France) through the
 71 French program on voluntary corpse donation to science. Among the donors, 16 were females and 13 were
 72 males (50 – 95 years old, 77.8 ± 11.4 , mean \pm SD). The nominal specimen size was $3 \times 4 \times 5$ mm³ in radial
 73 (axis 1), circumferential (axis 2) and axial directions (axis 3), respectively, defined by the anatomical shape
 74 of the femoral diaphysis. Details of sample preparation can be found in Cai et al. [39].

75 2.2. Bulk elasticity of the bone specimens

Cortical bone was assumed to be a transversely isotropic material [40, 41]; using Voigt notation, the
 matrix form of the stiffness tensor writes

$$\mathbf{C} = \begin{pmatrix} C_{11} & C_{12} & C_{13} & 0 & 0 & 0 \\ C_{12} & C_{11} & C_{13} & 0 & 0 & 0 \\ C_{13} & C_{13} & C_{33} & 0 & 0 & 0 \\ 0 & 0 & 0 & C_{44} & 0 & 0 \\ 0 & 0 & 0 & 0 & C_{44} & 0 \\ 0 & 0 & 0 & 0 & 0 & C_{66} \end{pmatrix}, \quad (1)$$

76 where, $C_{12} = C_{11} - 2C_{66}$ and (1–2) is the isotropy plane; C_{11} and C_{33} are the longitudinal stiffness constants,
 77 C_{12} and C_{13} are the off-diagonal stiffness constants; and C_{44} and C_{66} are the shear stiffness constants.

78 In the present study, we use already published anisotropic elasticity data of cortical bone specimens
 79 measured with RUS [39]. The main sources of experimental errors are related to the irregularities of spec-
 80 imen’s geometry and the uncertainties on the values of extracted resonant frequencies. These errors have
 81 been documented in a previous study and are of the order of 1.7% for shear stiffness constants, 3.1% for
 82 longitudinal and off-diagonal stiffness constants [42]. Hereafter, the stiffness constants measured by RUS are
 83 referred to as C_{ij}^{EXP} .

84 2.3. Bone microstructure and degree of mineralization

85 Degree of mineralization of bone (DMB) and vascular porosity (ϕ) data used in this work has been
 86 published and was obtained following the imaging protocol described in detail in Cai et al. [39]. Briefly,
 87 specimens were imaged with a pixel size of $6.5 \mu\text{m}$ with synchrotron radiation micro-computed tomography
 88 (SR- μCT) at the European Synchrotron Radiation Facility (ESRF) using a SR- μCT setup based on a 3-D
 89 parallel beam geometry acquisition [43, 44]. The calibrated gray levels of each specimen were converted into
 90 volumetric DMB as detailed in Nuzzo et al. [45].

91 For the purpose of homogenization (see Section 2.5), the 3D volume of each specimen was slightly rotated
 92 using Fiji [46] so that the image reference frame coincides with the orientation of the specimen’s faces. In
 93 each specimen, the largest possible rectangular parallelepiped volume of interest (VOI) was selected manually
 94 to achieve the largest available volume (average size about $2.8 \times 3.9 \times 4.8 \text{ mm}^3$). The VOIs were binarized
 95 by simple thresholding treating the void volumes as a solid and the bone phase as a background, from which
 96 ϕ of each specimen was measured. Finally, the voxel size was downsampled to $35 \mu\text{m}$ after having conducted
 97 convergence tests reported in Appendix B. The average total number of voxels in each VOI was about 1.2
 98 million.

99 2.4. Bone matrix acoustic impedance

100 A subset of 23 specimens (all from the lateral quadrant) were measured with a custom SAM to provide
 101 an independent measurement of tissue elastic properties for comparison with the results of inverse homoge-
 102 nization. The SAM operating with a spherically focused 100-MHz transducer (KSI 100/60°, Krämer Scientific
 103 Instruments, Herborn, Germany) was used to probe the acoustic impedance normal to the samples surfaces
 104 according to the measurement procedure extensively detailed in [47]. Calibrated impedance (Z) maps were
 105 obtained with a lateral resolution of $19.8 \mu\text{m}$ for the faces perpendicular to radial and axial directions. The
 106 Z -maps were segmented allowing the separation of vascular porosity and bone EVM. The acoustic impedance
 107 of the matrix was determined from the segmented maps of the specimens. The small pores (Volkmann’s
 108 canal, osteocyte lacunae) could not be resolved so that they contributed to the probed bulk matrix properties.

Matrix impedance in the probing direction, denoted $Z_i (i = 1, 3)$, was defined as the mean value of the
 Z -map scanned in the face of direction i . Matrix impedance was then converted to EVM stiffness using the
 following equation:

$$C_{ii}^Z = \frac{Z_i}{\rho_t}, \quad (2)$$

109 where $\rho_t = 1.12 + 0.73 \cdot \text{DMB} - 0.033 \cdot \text{DMB}^2$ is the tissue density converted from DMB values [48].

110 2.5. Forward problem: homogenization to simulate bulk stiffness

111 Each specimen's VOI was considered as a representative volume for homogenization containing two
112 homogeneous phases: vascular porosity and EVM. The elastic properties of the pore voxels were defined
113 with a bulk modulus of 2.2 GPa and a null shear modulus, corresponding to elastic properties of water.
114 The EVM voxels were allocated transverse isotropic elastic properties C_{ij}^m . The isotropy plane of the EVM
115 material was taken to be the plane 1 – 2. The terms C_{ij}^m are the unknowns of the inverse homogenization
116 problem.

117 The bulk stiffness tensor C_{ij}^{FFT} of each VOI was evaluated by the FFT homogenization method [37, 38].
118 Briefly, the bulk stiffness tensor is obtained after solving the local mechanical problem in the VOI (V)
119 consisting of the equilibrium equation, generalized Hooke's law as constitutive equation, compatibility of
120 the displacement field and boundary conditions. The phases are assumed to be perfectly bonded. The local
121 problem closed by periodic boundary conditions [49, 50] can be solved by the FFT-based numerical approach
122 proposed by Moulinec and Suquet [37].

123 The implementation of the method has been described in [9]. Note that no elastic symmetry assumption
124 was made for the calculation of the effective stiffness tensor. For the requirements of the present study, we
125 implemented a parallelized version of the FFT method. One loading in the FFT homogenization method
126 took around 50 iterations in our specimens and the effective stiffness tensor could be computed in about 1
127 minute on a workstation (CPU, Intel Xeon E5-2695 v3, 8 threads per loading).

128 For all VOIs, the values of the off-diagonal terms of the homogenized stiffness tensor C^{FFT} , which are
129 null in the case of orthotropy when the tensor is expressed in the material basis, were at least two orders of
130 magnitude smaller than the other terms. These off-diagonal terms were, therefore, disregarded, i.e., the 12
131 coefficients with index $kl = 11, 22, 33, 44, 55, 66, 12, 21, 13, 31, 23, 32$ were kept.

132 2.6. Inverse homogenization to recover EVM stiffness

133 The inverse homogenization consists in determining the matrix stiffness tensor \mathbf{C}^m which provides an op-
134 timum match between \mathbf{C}^{EXP} and $\mathbf{C}^{\text{FFT}}(\mathbf{C}^m)$. Two approaches have been implemented: (1) The 'calibration
135 approach' assumes that one mesoscale coefficient C_{ij}^{FFT} is fully determined by the porous microstructure and
136 its EVM counterpart C_{ij}^m . (2) The 'optimization approach' determines the EVM stiffness constants without
137 such assumption, i.e., it accounts for the possible dependence of one term of the mesoscale tensor C_{ij}^{FFT} on
138 all EVM stiffness constants. The 'calibration approach' is straightforward and less demanding in terms of
139 computational resources, but intrinsically less precise to determine C_{ij}^m . We found that the two approaches
140 lead to only slightly different results. Only the details and the results of the 'optimization approach' are
141 detailed in the paper. The methodology and results of the 'calibration approach' are reported in Appendix
142 A.

EVM stiffness constants \mathbf{C}^m of each specimen were obtained by minimizing the objective function defined as the root-mean-square-error (RMSE) between experimental and homogenized bulk stiffness constants. That is, for each specimen, we solve

$$RMSE(\mathbf{C}^m) = \sqrt{\frac{1}{12} \sum_{kl} \left(\frac{C_{kl}^{EXP} - C_{kl}^{FFT}(\mathbf{C}^m)}{C_{kl}^{EXP}} \right)^2} \times 100\%, \quad (3)$$

143 Note that the 12 non-zero coefficients (labeled by kl) are used in eq. 3. The Nelder-Mead Simplex Method
 144 implemented in Matlab Optimization Toolbox Release 2017b (MathWorks, Natick, MA), which does not
 145 require derivative information, was used to solve the minimization problem. The iterative solver stopped
 146 when, for two consecutive iterations, both the difference of the objective function values (eq. 3), and the
 147 difference of the norms of C_{ij}^m , were smaller than 0.001. For most of the specimens, the optimization stopped
 148 after about 130 iterations which costed about 130 minutes per specimen. The optimization procedure was
 149 initialized at the values (\mathbf{C}^{m0}) of $C_{11}^{m0} = 24.4$ GPa, $C_{33}^{m0} = 33.5$ GPa, $C_{13}^{m0} = 14.7$ GPa, $C_{44}^{m0} = 6.9$
 150 GPa, $C_{66}^{m0} = 5.4$ GPa. These values, reported in [9], were found by minimizing the differences between
 151 experimental and homogenized stiffness constants for the entire collection of specimens.

152 2.7. Estimation of the precision of inverse homogenization to recover EVM stiffness

153 \mathbf{C}^m is recovered from experimental elasticity data and the images of each specimen's microstructure.
 154 The images have a high contrast and a high resolution so that there is little concern about the precision of
 155 the reconstruction of the pore vascular network. The method of solution used for the forward problem yields
 156 the exact solution of the continuum mechanics problem with a controlled numerical precision. It follows
 157 that the uncertainties on C_{ij}^m mostly stem from the experimental uncertainties on C_{ij}^{EXP} . We conducted
 158 an error propagation analysis using Monte-Carlo (MC) simulations to estimate the errors on C_{ij}^m due to the
 159 uncertainties on C_{ij}^{EXP} .

Three specimens with porosities covering the entire porosity range (5.0%, 9.9% and 15.4%) were selected
 for the MC simulations to account for an expected dependence of the error on porosity. The experimental
 uncertainties on stiffness constants were modeled with independent normal distributions. The distribu-
 tions were centred at mesoscale stiffness values obtained from the FFT homogenization of each of the three
 specimen's VOI with EVM stiffness \mathbf{C}^{m0} . The width of the distributions were consistent with the typi-
 cal experimental uncertainties for longitudinal and off-diagonal stiffness constants (SD of 3.0%) and shear
 stiffness constants (SD of 1.5%). A set of 1000 independent realizations of mesoscale stiffness tensors were
 drawn from the normal distributions. The EVM stiffness C_{ij}^m was calculated for each realization of mesoscale
 stiffness tensor using inverse homogenization and compared with \mathbf{C}^{m0} to calculate the relative error on each
 coefficient, defined as

$$\delta C_{ij}^m = (C_{ij}^m - C_{ij}^{m0}) / C_{ij}^{m0} \times 100\%, \quad (4)$$

160 *2.8. Data analysis*

161 Linear least squares regressions were conducted to analyze the relationships between elastic properties,
 162 impedance and DMB. Pearson’s correlation coefficient are reported. Normality of the distributions of the
 163 C_{ii}^m and C_{ii}^Z was verified using the ShapiroWilk test. Paired t-test was used to test if C_{ii}^m and C_{ii}^Z were
 164 different. The level of significance for all the tests was set to $p = 0.05$.

165 **3. Results**

166 *3.1. Descriptive statistics*

167 The specimens of one subject with a porosity higher than 30% was not included in the analysis. Another
 168 specimen was broken during sample preparation. Finally 55 specimens were used for this study.

169 The bulk elasticity of five specimens with a porosity larger than 14.5% were found to be slightly or-
 170 thotropic due to the shape of the pore network [9]. Precisely, the relative difference between C_{22}^{FFT} and
 171 C_{11}^{FFT} , or between C_{44}^{FFT} and C_{55}^{FFT} exceeded 3% for these five specimens. This violates the assumption of a
 172 transverse isotropic material used to process RUS measurements. Despite the fact that, for these specimens,
 173 the inverse homogenization optimization lead to a relatively good fit with a RMSE (eq. 3) between 1 and
 174 2%, these specimens were discarded. The results presented below are consequently given for 50 specimens.

175 Experimental stiffness constants, porosity, DMB and matrix impedance are summarized in Table 1. The
 176 coefficient of variation (CV) of DMB was about 2% which is smaller than the CV of Z_i (4.2 – 4.3%) and
 177 C_{ij}^{EXP} (7 – 14%).

Table 1: The average, SD and range of the experimental data of the stiffness constants (C_{ij}^{EXP}), porosity (ϕ), DMB (ρ_m) and matrix acoustic impedance (Z_i). Note that Z_i was measured on 23 specimens from the lateral quadrant.

	C_{11}^{EXP} (GPa)	C_{33}^{EXP} (GPa)	C_{13}^{EXP} (GPa)	C_{44}^{EXP} (GPa)	C_{66}^{EXP} (GPa)
Mean±SD	20.1 ± 1.5	29.5 ± 1.3	12.0 ± 0.9	6.0 ± 0.4	4.5 ± 0.5
Range	16.9 – 23.8	25.7 – 32.1	9.3 – 14.1	4.7 – 6.9	3.5 – 5.9
	ϕ (%)	ρ_m (g/cm ³)	Z_1 (Mrayl)	Z_3 (Mrayl)	
Mean±SD	6.5 ± 2.6	1.02 ± 0.02	6.8 ± 0.3	7.4 ± 0.3	
Range	1.8 – 12.1	0.95 – 1.06	6.2 – 7.5	6.9 – 8.1	

178 The RMSEs after inversion (eq. 3) were small, between 0.06 – 1.01% (Mean ± SD = 0.26 ± 0.19%).
 179 The EVM stiffness constants C_{ij}^m and the engineering moduli (obtained by inverting the stiffness tensor) are
 180 summarized in Table 2. The CVs of C_{ij}^m (3.0 – 7.1%, Table 2), EVM Young’s moduli (4.5 – 5.5%) and EVM
 181 Poisson’s ratios (5.3 – 11.5%) were greater than that of ρ_m (2%, Table 1).

182 *3.2. Error propagation analysis*

183 The distribution of each δC_{ij}^m (eq. 4) was found to be normally distributed (Shapiro-Wilk’s test). The
 184 results are summarized in Table 3. The offset (bias) of δC_{ij}^m from zero was small, less than 0.8%. The

Table 2: The mean, SD and range of the EVM stiffness constants C_{ij}^m and engineering moduli.

	C_{11}^m (GPa)	C_{33}^m (GPa)	C_{13}^m (GPa)	C_{44}^m (GPa)	C_{66}^m (GPa)
Mean±SD	24.5 ± 1.2	33.6 ± 1.1	14.7 ± 1.0	7.0 ± 0.3	5.4 ± 0.4
Range	21.7 – 27.5	31.4 – 36.2	12.1 – 16.7	6.1 – 7.5	4.5 – 6.3
	E_1^m (GPa)	E_3^m (GPa)	ν_{23}^m	ν_{31}^m	ν_{12}^m
Mean±SD	15.1 ± 0.8	22.4 ± 1.0	0.26 ± 0.02	0.38 ± 0.02	0.41 ± 0.03
Range	13.2 – 17.0	20.3 – 24.9	0.19 – 0.31	0.34 – 0.41	0.32 – 0.48

185 uncertainty characterized by SDs of δC_{ij}^m were between 3.1–4.7% for longitudinal and off-diagonal coefficients
186 and 1.5–1.9% for shear coefficients (Table 3). These uncertainties are comparable with the SDs of the errors
187 modeled in MC simulations and corresponding to experimental uncertainty on C_{ij}^{EXP} . We noted that the
188 SD of δC_{ij}^m increases as porosity increases.

Table 3: The errors (Mean±SD in %) on EVM stiffness constants affected by the experimental errors on the bulk stiffness constants. Calculation were performed for 3 specimens of 5.0%, 9.9% and 15.4% porosity.

	$\phi = 5.0\%$	$\phi = 9.9\%$	$\phi = 15.4\%$
δC_{11}^m	0.21 ± 3.49	-0.01 ± 3.96	-0.76 ± 4.66
δC_{33}^m	0.02 ± 3.05	-0.09 ± 3.06	-0.17 ± 2.99
δC_{13}^m	0.17 ± 3.12	0.03 ± 3.55	-0.35 ± 3.90
δC_{44}^m	-0.12 ± 1.49	-0.07 ± 1.58	0.08 ± 1.59
δC_{66}^m	-0.16 ± 1.62	0.07 ± 1.70	0.69 ± 1.87

189 3.3. Comparison between EVM stiffness derived by RUS and SAM

190 SAM provides a direct assessment of acoustic impedance Z which is a good proxy for stiffness. Impedance
191 can be converted to stiffness C_{ii}^Z according to eq. 2 which can be directly compared to C_{ii}^m . EVM longitudinal
192 stiffness constants evaluated by inverse homogenization and SAM are compared in Table 4. The values of
193 C_{ii}^m and C_{ii}^Z were significantly different ($p < 0.002$). The mean value of C_{11}^m was about 5.1% smaller than
194 that of C_{11}^Z , while the mean value of C_{33}^m was about 10.2% greater than that of C_{33}^Z . C_{ii}^Z exhibited a greater
195 variability (CV was about 8%) compared to C_{ii}^m (CV between 3–5%). No significant correlation was found
196 between C_{11}^m and C_{11}^Z , nor between C_{33}^m and C_{33}^Z .

Table 4: Comparison between EVM stiffness measured by RUS and SAM.

	Mean±SD	Range
C_{11}^m (GPa)	24.0 ± 1.2	21.7 – 26.7
C_{11}^Z (GPa)	25.4 ± 2.0	21.5 – 30.6
C_{33}^m (GPa)	33.5 ± 1.1	31.4 – 36.2
C_{33}^Z (GPa)	30.4 ± 2.4	25.8 – 35.3

197 Figure 1 and 2 summarize the relationships observed between C_{ij}^m and Z_i . The CV of C_{ij}^m (3.0 – 7.1%)
 198 is comparable with that of Z_i . Significant positive correlations were observed between Z_1 and the C_{44}^m , C_{66}^m
 199 ($0.52 < r < 0.60$, Figure 1), and between Z_3 and C_{44}^m ($r = 0.42$, Figure 2). Trends of positive (not significant)
 200 correlations were also observed between Z_1 and C_{11}^m , C_{33}^m and C_{13}^m ($0.34 < r < 0.38$, Figure 1), and between
 201 Z_3 and C_{66}^m ($r = 0.36$, Figure 2).

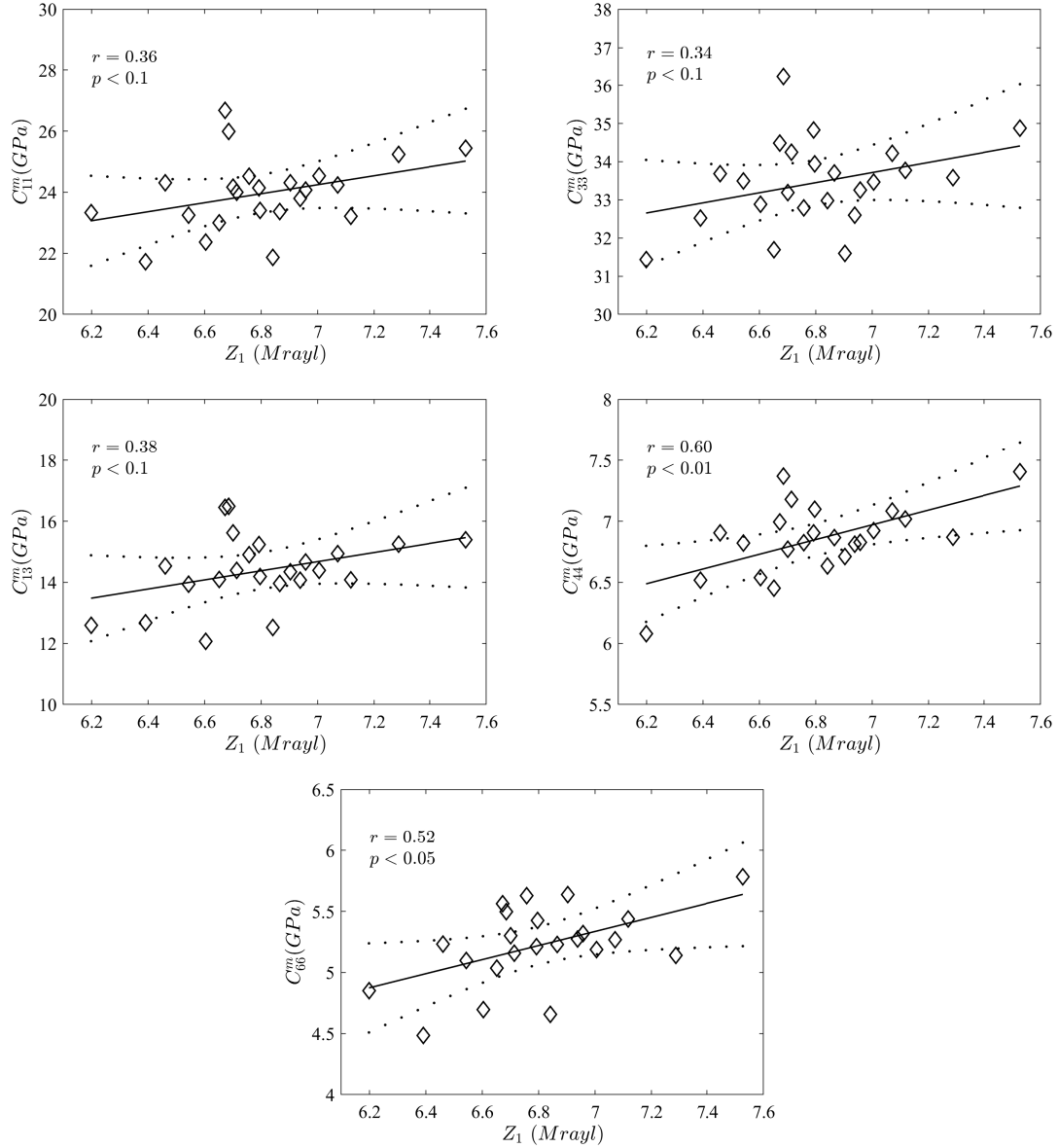


Figure 1: Relationships between Z_1 and C_{ij}^m , and the corresponding linear regression model (solid line) with the 95% CI (dot line). r is the Pearson's correlation coefficient.

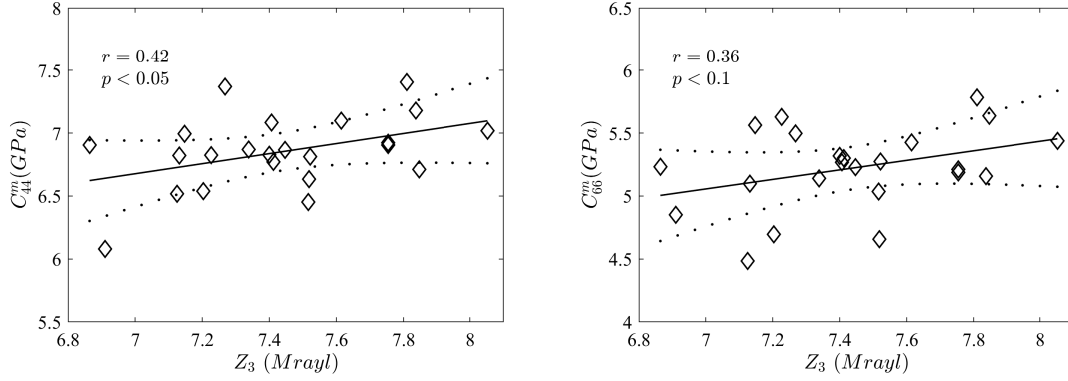


Figure 2: Relationships between Z_3 and C_{44}^m , C_{66}^m , and the corresponding linear regression model (solid line) with the 95% CI (dot line). r is the Pearson's correlation coefficient.

202 3.4. Variations of EVM stiffness with DMB

203 Significant correlations were observed between ρ_m and C_{44}^m , C_{66}^m ($0.65 < r < 0.70$, Figure 3). The data
 204 suggest a positive relationship might exist between C_{11}^m , C_{33}^m , C_{13}^m and ρ_m , but the correlations ($0.24 < r <$
 205 0.27) were not significant. Also, ρ_m positively correlated with E_1^m , ν_{23}^m and ν_{31}^m ($0.32 < r < 0.59$), and
 206 negatively with ν_{12}^m ($r = -0.61$) (Figure 4). The linear regression equations between ρ_m and EVM stiffness
 207 constants are given in Table 5.

Table 5: Empirical laws between ρ_m and C_{ij}^m .

Laws	
C_{11}^m	$14.96 \times \rho_m + 9.28$
C_{33}^m	$13.99 \times \rho_m + 19.39$
C_{13}^m	$11.79 \times \rho_m + 2.69$
C_{44}^m	$8.82 \times \rho_m - 2.02$
C_{66}^m	$11.13 \times \rho_m - 5.97$

208 4. Discussion

209 In this work, we introduced an inverse homogenization approach to evaluate the anisotropic elastic
 210 properties C_{ij}^m of cortical bone EVM. The approach uses a measurement of the transverse isotropic stiffness
 211 tensor at the mesoscale (with RUS) and assumes that the EVM is itself transverse isotropic. The EVM
 212 stiffness values obtained are to be understood as 'mean' values representative of the entire volume of the
 213 specimen as the forward problem (homogenization) assumes a homogeneous EVM throughout the specimen's
 214 volume. One key aspect of the work is that the homogenization is performed with the real vascular pore
 215 structure obtained with the state-of-the-art 3D μ -CT imaging. Also, the VOI used as a representative
 216 volume element for homogenization almost matches the specimen volume assessed by RUS, enabling a direct

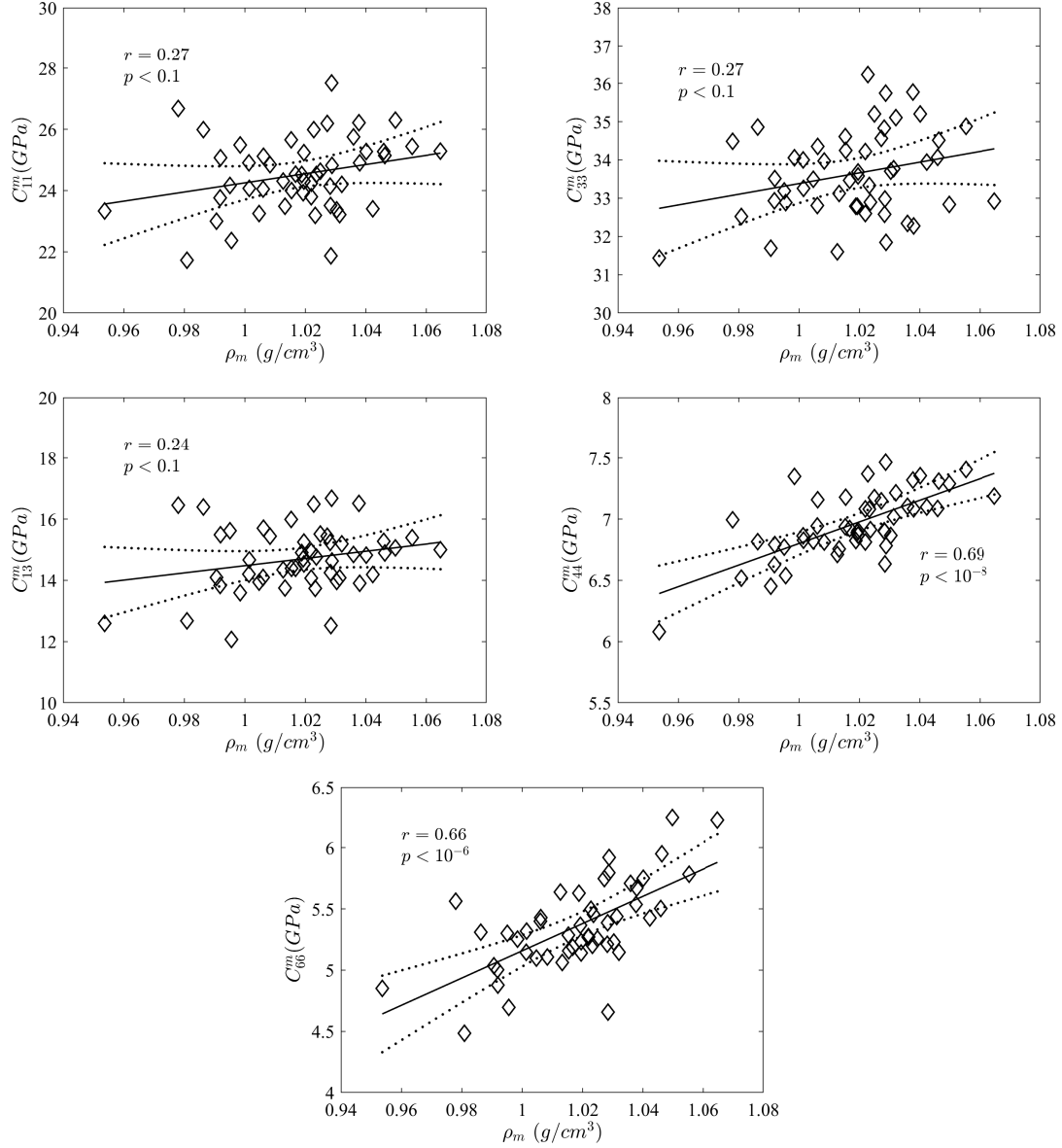


Figure 3: Relationships between ρ_m and C_{ij}^m , and the corresponding linear regression model (solid line) with the 95% CI (dot line). r is the Pearson's correlation coefficient.

217 comparison between predicted and measured mesoscale stiffness. It is noteworthy that the method provides
 218 the complete elastic tensor, from which the engineering moduli (i.e., Young's moduli, shear moduli and
 219 Poisson's ratios) can be obtained.

220 The fine knowledge of experimental errors on the stiffness constants measured by RUS [42] allows per-
 221 forming a realistic estimation of the errors on C_{ij}^m determined by inverse homogenization. The magnitude
 222 of the errors (SD= 1.5 – 1.9% for shear coefficients and SD = 3.1 – 4.7% for longitudinal and off-diagonal
 223 coefficients, Table 3) were close to the errors on the bulk stiffness constants measured with RUS. Note that
 224 the errors on C_{11}^m were a bit larger than on C_{33}^m , which may be explained by the fact that small anisotropy in

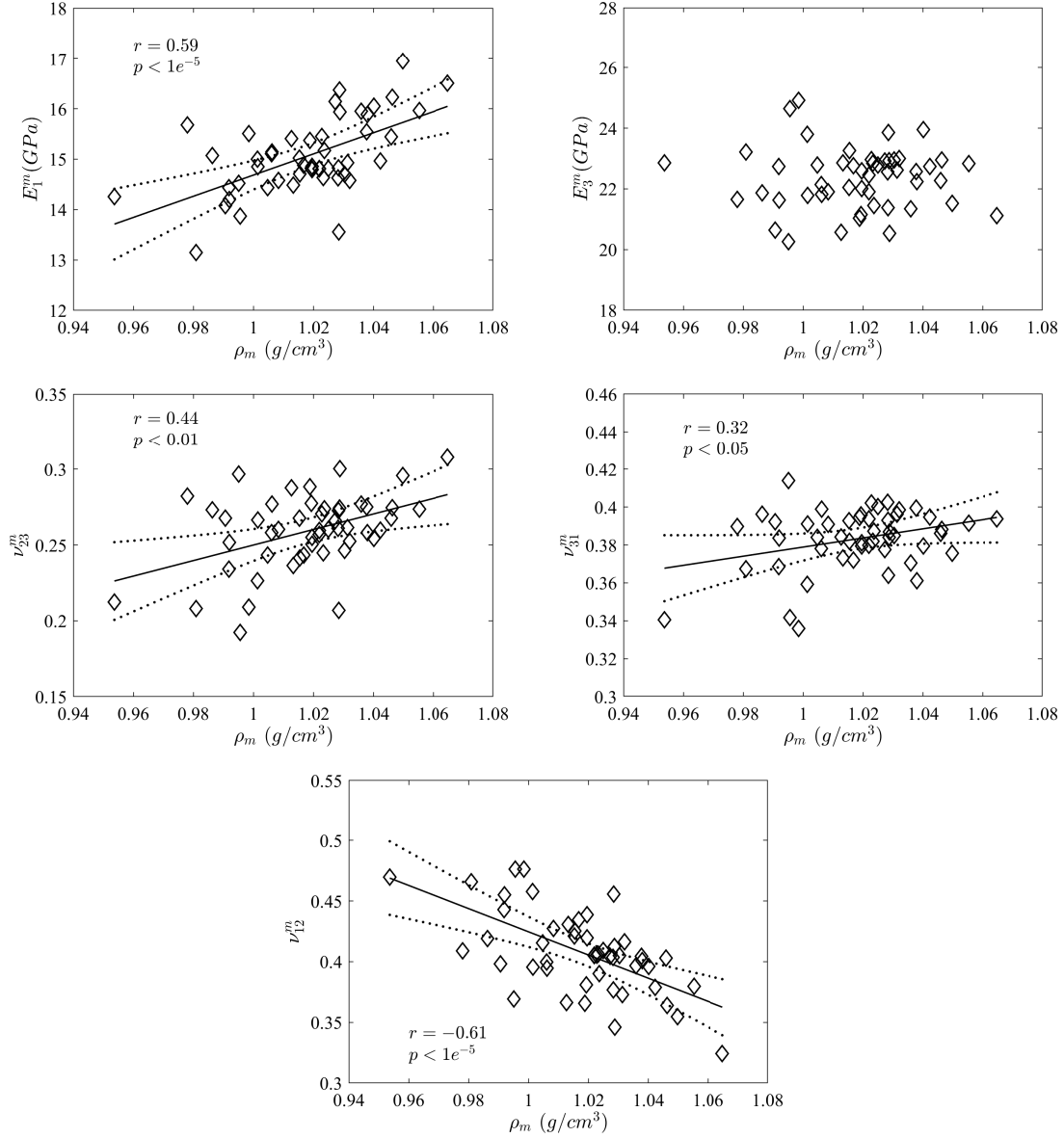


Figure 4: Relationships between ρ_m and EVM Young's moduli and Poisson's ratio, and the corresponding linear regression model (solid line) with the 95% CI (dot line). r is the Pearson's correlation coefficient.

225 the transverse plane is disregarded in the inverse homogenization process, forcing an 'artificial' adjustment
 226 of C_{11}^m . The errors on the EVM stiffness may be minimized by improving the precision and accuracy of RUS
 227 [42].

228 The average values of EVM stiffness constants and Young's moduli agreed well with the values reported
 229 in previous studies measured on human femoral bone as well [19, 24, 32] (Table 6). These values from
 230 the literature were evaluated by various approaches, including acoustic, indentation and micromechanical
 231 model-based methods. Specifically, the average values of C_{33}^m , C_{44}^m , C_{66}^m and all the engineering moduli
 232 fell inside the range of values measured by SAM and nano-indentation. For C_{11}^m and the two off-diagonal

233 coefficients C_{13}^m and C_{12}^m , our values were a bit higher. As far as we are aware, only two articles reported the
 234 measurement of the entire anisotropic elastic tensor of the EVM [19, 32]. The method used by Lakshmanan
 235 et al. [32], based on SAM measurements relies on empirical laws (relating acoustic impedance to several
 236 stiffness constants) and idealized micromechanical models (for the off-diagonal coefficients) to retrieve the
 237 elastic tensor. The method used by Franzoso and Zysset [19], based on nano-indentation measurements, uses
 238 an indenter shape-dependent model [51] and a fabric tensor incorporating important assumptions (fibers
 239 organization and simplified intrinsic material model).

240 For instance, our data and the data from [32] respect the inequality relation $\nu_{23} < \nu_{31} < \nu_{12}$ noted
 241 in Cowin [52], while not the data from Franzoso and Zysset [19]. In our approach, we only assume transverse
 242 isotropic elastic symmetry for EVM. Furthermore, we provide data for a relatively large number of subjects.

Table 6: Comparison between the bone EVM elastic properties found in this work and in previous studies. The values are summarized as mean \pm SD except those converted by the mean values of the coefficients (elastic tensor to Engineering moduli or conversely). Franzoso: Franzoso and Zysset [19]; Lakshmanan: Lakshmanan et al. [32]; Turner: [24].

	Acoustic		Nano-indentation		
	This study	Lakshmanan	Turner		Franzoso
C_{11}^m (GPa)	24.5 ± 1.2	21.9 ± 2.1	22.4 ± 0.8	—	14.3
C_{33}^m (GPa)	33.6 ± 1.1	29.9 ± 5.0	28.3 ± 0.3	—	38.6
C_{13}^m (GPa)	14.7 ± 1.0	9.7 ± 1.6	—	—	12.3
C_{12}^m (GPa)	13.8 ± 0.9	9.2 ± 1.5	—	—	10.3
C_{44}^m (GPa)	7.0 ± 0.3	6.7 ± 1.2	—	—	7.7 ± 0.5
C_{66}^m (GPa)	5.4 ± 0.4	6.4	—	—	4.7 ± 0.4
E_1^m (GPa)	15.1 ± 0.8	16.8	14.9 ± 0.5	16.6 ± 0.3	9.2 ± 0.6
E_3^m (GPa)	22.4 ± 1.0	23.8	20.6 ± 0.2	23.5 ± 0.2	24.7 ± 2.7
ν_{23}^m	0.26 ± 0.02	0.22	—	—	0.29 ± 0.02
ν_{31}^m	0.38 ± 0.02	0.31	—	—	0.56 ± 0.02
ν_{12}^m	0.41 ± 0.03	0.32	—	—	0.25 ± 0.01

243 SAM provided impedance data and combined with a model to derive mass density from DMB, provided
 244 an independent measure of EVM stiffness. SAM is seemingly the most appropriate technique to perform a
 245 comparison with our EVM stiffness values because it scans entire surfaces of the cuboid specimens; SAM data
 246 can then be averages, yielding values directly comparable with C_{ij}^m derived from inverse homogenization.
 247 We found significant correlations between impedance data and EVM shear stiffness (Figure 1) and 2).
 248 For the other stiffness constants, the data suggest a relationship might exist with acoustic impedance but
 249 no significant correlations were observed. The differences between the mean values of the longitudinal
 250 EVM stiffness evaluated by inverse homogenization and derived from SAM were relatively small ($< 10.2\%$,
 251 Table 4) considering that the two methodologies are different. However, stiffness derived with SAM and
 252 inverse homogenization were not correlated. The low and non-significant correlation may in part be due to
 253 the fact that only 23 among 55 specimens were measured with SAM.

254 The reason for the lack of correlation is likely due to experimental errors of both techniques. RUS
255 is intrinsically more accurate for shear stiffness compared to longitudinal stiffness [53, 54], which would
256 explain that correlations are found between impedance and shear stiffness. Note that, SAM requires a
257 flat and polished surface to measure the acoustic impedance. This is obtained by a manual polishing of
258 the specimens which is especially difficult to realize when the sample size is small, as is the case for our
259 specimens (Z_1 and Z_3 were measured on the $4 \times 5 \text{ mm}^2$ and $3 \times 4 \text{ mm}^2$ surfaces, respectively). In addition,
260 SAM is a surface measurement, whereas the C_{ij}^m evaluated by inverse homogenization are representative of
261 the entire volume of a specimen. The relatively narrow range of variation of the EVM stiffness, combined
262 with measurement errors are likely to weaken correlations.

263 Significant correlations between DMB (averaged in the specimen’s volume) and EVM shear stiffness (Fig-
264 ure 3), and most of the EVM engineering moduli (Figure 4) were observed, which has not been reported
265 before. Similar to the observation for impedance data, the correlation between DMB and the EVM longitu-
266 dinal stiffness were not significant. This is consistent with the magnitude of the errors in stiffness measured
267 by RUS as previously mentioned. Furthermore, opposite correlations between DMB and the Poisson’s ratios
268 were observed suggesting different deformation behavior in different directions may exist at the tissue level
269 as bone is mineralizing, which may be interesting to investigate in the future. Note that the repeatability of
270 the DMB measured by SR- μ CT varying beam energy was reported to be as small as 0.26% using the same
271 setup on beamline ID 19 at ESRF [55], which may be a reason why correlations with stiffness are found
272 although the range of variation of DMB is small.

273 The bone specimens used in this study are from donors with undocumented medical history. Overall,
274 the presented EVM stiffness data set (Table 2) may only represent a group of elderly population without
275 a specific bone pathology. As expected for such a population, the EVM stiffness values vary in a relatively
276 small range (from 4.8% to 15.4%). This data may be used as a reference data set to compare with EVM
277 stiffness in bone pathology.

278 Some limitations in this study should be mentioned. Although the entire EVM stiffness tensor of the
279 specimens is provided in this work, the accuracy of the values need further investigation. The comparison with
280 SAM-derived stiffness shows a relatively good agreement, and the comparison with the values obtained from
281 nanoindentation indicates that the values of EVM stiffness obtained with inverse homogenization are in the
282 expected range. Most importantly, the correlations between some stiffness constants and DMB demonstrate
283 that the proposed method is sufficiently precise to probe small differences of elasticity due to small changes
284 of DMB.

285 We assumed that the EVM is homogeneous. In reality, bone matrix mechanical properties are hetero-
286 geneous depending on the local variations of the degree of mineralization (differences of elastic modulus
287 between osteonal and interstitial region in cortical bone[25, 56]) and microfibril orientation [26]. Though it
288 has been shown in trabecular bone that the bulk elastic properties only changed about 2% considering an
289 heterogeneous model [57], the effect of neglecting tissue heterogeneity has not been quantified in cortical

290 bone.

291 We also assumed that the EVM stiffness is transverse isotropic. This was a necessary assumption because
292 the RUS experimental data itself was obtained with this assumption at the mesoscale level. This assumption
293 proved to be valid for most of the specimens, however it may not be valid for specimens taken at other
294 anatomical sites.

295 5. Conclusion

296 To conclude, we introduced an inverse homogenization method to evaluate cortical bone EVM anisotropic
297 elastic properties. Our approach provides the entire EVM stiffness tensor with a precision of a few percent.
298 The EVM stiffness tensor is provided for 50 specimens from 26 elderly donors exhibiting the range of vari-
299 ation for this population. The present work is unprecedented documentation of EVM anisotropic elasticity.
300 One important perspective is the quantification of *in situ* strains of the EVM under loading which has
301 consequences for the mechanotransduction process.

302 Acknowledgment

303 This work has received financial support from the Agency National Research under the ANR-13-BS09-
304 0006 MULTIPS project. The authors would like to thank ESRF for the access of beamline at ID 19 and 17
305 and the help from Cécile Olivier and Françoise Peyrin for performing SR- μ CT experiments.

306 Appendix A. Calibration approach

307 From several preliminary tests, we found that the coupling between C_{ij}^{FFT} and its counterpart C_{ij}^m
308 (e.g., between C_{11}^{FFT} and C_{11}^m) is much stronger than the other EVM stiffness constants which means that
309 specimen-specific relationships can be built between them. Specifically, the relationship between C_{11}^{FFT} (as
310 an example) and C_{11}^m was established by varying the values of C_{11}^m starting from C_{11}^{m0} while fixing C_{33}^{m0} , C_{13}^{m0} ,
311 C_{44}^{m0} , C_{66}^{m0} (see Figure A.1). The range of variations were $C_{11}^{m0} \pm 10$ GPa, $C_{33}^{m0} \pm 12$ GPa, $C_{13}^{m0} \pm 6$ GPa,
312 $C_{44}^{m0} \pm 4$ GPa and $C_{66}^{m0} \pm 3$ GPa (5 evenly distributed points in the interval for each coefficient), respectively.
313 Then, the C_{11}^{EXP} was projected to C_{11}^m given the established relationship (Figure A.1). It costed about
314 30 minutes ($5 \times 6 = 30$ forward computations) to calculate EVM stiffness constants of a specimen in the
315 calibration approach.

316 The RMSE (eq. 3) was also calculated for each specimen after \mathbf{C}^m was obtained to compare with the
317 ones from optimization approach. The RMSEs from the calibration approach were between 0.12 – 2.52%
318 (Mean \pm SD = $0.76 \pm 0.46\%$) greater than that from the optimization approach in general which is expected.
319 The optimization approach takes all the coupling between the coefficients into account, i.e., it allows more
320 degrees of freedom. Therefore, it is expected that the optimization approach would produce smaller RMSEs.

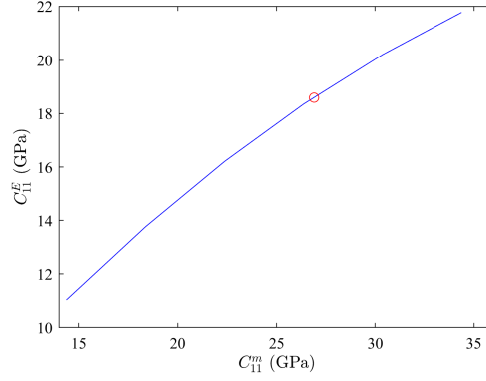


Figure A.1: An example of a specimen-specific relationship (solid curve) between C_{11}^{FFT} and C_{11}^m . The latter was projected (circle) by C_{11}^{EXP} using the relationship.

321 Bland-Altman's plots between the C_{ij}^m from the two approaches showed that only a small bias existed for
 322 C_{11}^m (0.15 GPa), but not for the other coefficients (< 0.07 GPa) and the relative differences are quite small
 323 (CV was between 0.35 – 0.96%) compared to experimental errors. Therefore, one can conclude that there is
 324 no significant difference between the two inverse homogenization approaches.

325 Appendix B. Convergence study

326 The convergence study was carried out on the three specimens mentioned in Section 2.7 whose original
 327 pixel size (ps) of the 3D images was $6.5 \mu\text{m}$.

328 Appendix B.1. Forward problem

329 The convergence study for the forward problem was mainly used to determine the pixel size for the VOIs.
 330 Details can be found in Cai et al. [9] (Appendix B.2).

331 Appendix B.2. Inverse problem

The ps of the images of each specimen was increased to 10, 15, 20, 25, 30 and $35 \mu\text{m}$, respectively, in order to study how the image resolution affects the result of the inverse homogenization. The bulk stiffness constants of each specimen, calculated by the FFT homogenization when $ps = 10 \mu\text{m}$ and using C_{ij}^{m0} as the EVM stiffness constants, were used as the input. Applying the inverse homogenization on the images at the other ps ($15 - 35 \mu\text{m}$) for each specimen, the bias between EVM stiffness constants $C_{ij}^{m,ps}$ evaluated at different ps and C_{ij}^{m0} was quantified by the RMSE denoted below:

$$RMSE(ps) = \sqrt{\frac{1}{5} \sum_{ij} \left(\frac{C_{ij}^{m,ps} - C_{ij}^{m0}}{C_{ij}^{m0}} \right)^2} \times 100\% \quad (\text{B.1})$$

332 Results showed that when $ps \leq 35 \mu\text{m}$, all the RMSEs were less than 0.5%. Compared with the experimental
 333 errors in RUS, these values are smaller. To this end, $ps = 35 \mu\text{m}$ was considered as an appropriate value for
 334 the 3D images of the specimens and was chosen in this work.

335 **Appendix C. Validation of the inversion**

The effective stiffness constants C_{ij}^{FFT0} of all the 55 specimens were calculated by the FFT homogenization with the values C_{ij}^{m0} for bone EVM and the pixel size of the images was $35 \mu\text{m}$. Using C_{ij}^{FFT0} as the input, both the calibration and optimization approaches were implemented to calculate the EVM stiffness constants C_{ij}^m and the RMSE of each specimen was evaluated as:

$$RMSE = \sqrt{\frac{1}{5} \sum_{ij} \left(\frac{C_{ij}^m - C_{ij}^{m0}}{C_{ij}^{m0}} \right)^2} \times 100\% \quad (\text{C.1})$$

336 The results are depicted in Figure C.2 in which we observed that all the RMSE are less than 0.15% and
 337 0.018% for the calibration and optimization approaches, respectively, and most are less than 0.05% and
 338 0.005%, which means that the inverse methods themselves are reliable.

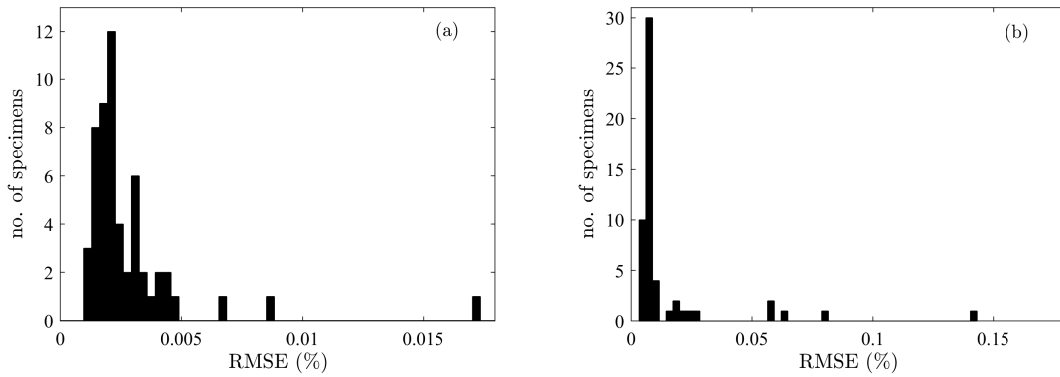


Figure C.2: Histogram of the RMSE (eq. C.1) of the specimens from the (a) optimization and (b) calibration approaches.

339 **References**

340 [1] J. D. Currey, *Bones: structure and mechanics*, Princeton university press, Princeton, 2002.

341 [2] Q. Grimal, K. Raum, A. Gerisch, P. Laugier, A determination of the minimum sizes of representative
 342 volume elements for the prediction of cortical bone elastic properties, *Biomechanics and modeling in
 343 mechanobiology* 10 (2011) 925–937.

344 [3] J. Y. Rho, L. Kuhn-Spearing, P. Zioupos, Mechanical properties and the hierarchical structure of bone,
 345 *Medical engineering and physics* 20 (1998) 92–102.

346 [4] A. Fritsch, C. Hellmich, 'universal' microstructural patterns in cortical and trabecular, extracellular
 347 and extravascular bone materials: Micromechanics-based prediction of anisotropic elasticity, *Journal of
 348 Theoretical Biology* 244 (2007) 597–620.

- 349 [5] Q. Grimal, G. Rus, W. J. Parnell, P. Laugier, A two-parameter model of the effective elastic tensor for
350 cortical bone, *Journal of biomechanics* 44 (2011) 1621–1625.
- 351 [6] W. J. Parnell, M. Vu, Q. Grimal, S. Naili, Analytical methods to determine the effective mesoscopic
352 and macroscopic elastic properties of cortical bone, *Biomechanics and modeling in mechanobiology* 11
353 (2012) 883–901.
- 354 [7] C. Hellmich, F.-J. Ulm, L. Dormieux, Can the diverse elastic properties of trabecular and cortical bone
355 be attributed to only a few tissue-independent phase properties and their interactions?, *Biomechanics
356 and modeling in mechanobiology* 2 (2004) 219–238.
- 357 [8] A. P. Baumann, J. M. Deuerling, D. J. Rudy, G. L. Niebur, R. K. Roeder, The relative influence of
358 apatite crystal orientations and intracortical porosity on the elastic anisotropy of human cortical bone,
359 *Journal of biomechanics* 45 (2012) 2743–2749.
- 360 [9] X. Cai, R. Brenner, L. Peralta, C. Olivier, P.-J. Gouttenoire, C. Chappard, F. Peyrin, D. Cassereau,
361 P. Laugier, Q. Grimal, Homogenization of cortical bone reveals that the organization and shape
362 of pores marginally affect elasticity, *Journal of The Royal Society Interface* 16 (2019) 20180911.
363 doi:10.1098/rsif.2018.0911.
- 364 [10] H. Hemmatian, A. D. Bakker, J. Klein-Nulend, G. H. van Lenthe, Aging, osteocytes, and mechan-
365 otransduction, *Current Osteoporosis Reports* (2017) 1–11.
- 366 [11] M. Granke, Q. Grimal, A. Saïed, P. Nauleau, F. Peyrin, P. Laugier, Change in porosity is the major
367 determinant of the variation of cortical bone elasticity at the millimeter scale in aged women, *Bone* 49
368 (2011) 1020–1026.
- 369 [12] C. Hoffer, K. Moore, K. Kozloff, P. Zysset, M. Brown, S. Goldstein, Heterogeneity of bone lamellar-level
370 elastic moduli, *Bone* 26 (2000) 603–609.
- 371 [13] J. D. Currey, Role of collagen and other organics in the mechanical properties of bone, *Osteoporosis
372 International* 14 (2003) S29–S36.
- 373 [14] B. Grabner, W. Landis, P. Roschger, S. Rinnerthaler, H. Peterlik, K. Klaushofer, P. Fratzl, Age-and
374 genotype-dependence of bone material properties in the osteogenesis imperfecta murine model (oim),
375 *Bone* 29 (2001) 453–457.
- 376 [15] Y. Bala, D. Farlay, G. Boivin, Bone mineralization: from tissue to crystal in normal and pathological
377 contexts, *Osteoporosis International* 24 (2013) 2153–2166.
- 378 [16] Y. Bala, B. Depalle, D. Farlay, T. Douillard, S. Meille, H. Follet, R. Chapurlat, J. Chevalier, G. Boivin,
379 Bone micromechanical properties are compromised during long-term alendronate therapy independently
380 of mineralization, *Journal of Bone and Mineral Research* 27 (2012) 825–834.

- 381 [17] S. Ma, E. L. Goh, A. Jin, R. Bhattacharya, O. R. Boughton, B. Patel, A. Karunaratne, N. T. Vo, R. At-
382 wood, J. P. Cobb, U. Hansen, R. L. Abel, Long-term effects of bisphosphonate therapy: perforations,
383 microcracks and mechanical properties., *Scientific reports* 7 (2017) 43399.
- 384 [18] P. K. Zysset, X. Edward Guo, C. Edward Hoffer, K. E. Moore, S. A. Goldstein, Elastic modulus and
385 hardness of cortical and trabecular bone lamellae measured by nanoindentation in the human femur,
386 *Journal of biomechanics* 32 (1999) 1005–1012.
- 387 [19] G. Franzoso, P. K. Zysset, Elastic anisotropy of human cortical bone secondary osteons measured by
388 nanoindentation, *Journal of biomechanical engineering* 131 (2009) 021001.
- 389 [20] K. Raum, I. Leguerney, F. Chandelier, M. Talmant, A. Saied, F. Peyrin, P. Laugier, Site-matched
390 assessment of structural and tissue properties of cortical bone using scanning acoustic microscopy and
391 synchrotron radiation μ ct, *Physics in medicine and biology* 51 (2006) 733.
- 392 [21] S. Yamada, S. Tadano, K. Fukasawa, Micro-cantilever bending for elastic modulus measurements of a
393 single trabecula in cancellous bone, *Journal of Biomechanics* 49 (2016) 4124–4127.
- 394 [22] J. Schwiedrzik, R. Raghavan, A. Bürki, V. LeNader, U. Wolfram, J. Michler, P. Zysset, In situ micropillar
395 compression reveals superior strength and ductility but an absence of damage in lamellar bone, *Nature*
396 *materials* 13 (2014) 740–747.
- 397 [23] K. W. Luczynski, A. Steiger-Thirsfeld, J. Bernardi, J. Eberhardsteiner, C. Hellmich, Extracellular
398 bone matrix exhibits hardening elastoplasticity and more than double cortical strength: evidence from
399 homogeneous compression of non-tapered single micron-sized pillars welded to a rigid substrate, *Journal*
400 *of the mechanical behavior of biomedical materials* 52 (2015) 51–62.
- 401 [24] C. H. Turner, J. Rho, Y. Takano, T. Y. Tsui, G. M. Pharr, The elastic properties of trabecular and
402 cortical bone tissues are similar: results from two microscopic measurement techniques, *Journal of*
403 *biomechanics* 32 (1999) 437–441.
- 404 [25] J.-Y. Rho, M. E. Roy, T. Y. Tsui, G. M. Pharr, Elastic properties of microstructural components of
405 human bone tissue as measured by nanoindentation, *Journal of biomedical materials research* 45 (1999)
406 48–54.
- 407 [26] M. Granke, A. Gourrier, F. Rupin, K. Raum, F. Peyrin, M. Burghammer, A. Saïed, P. Laugier, Mi-
408 crofibril orientation dominates the microelastic properties of human bone tissue at the lamellar length
409 scale, *PLoS One* 8 (2013) e58043.
- 410 [27] S. Schrof, P. Varga, B. Hesse, M. Schöne, R. Schütz, A. Masic, K. Raum, Multimodal correlative
411 investigation of the interplaying micro-architecture, chemical composition and mechanical properties of
412 human cortical bone tissue reveals predominant role of fibrillar organization in determining microelastic
413 tissue properties, *Acta Biomaterialia* 44 (2016) 51–64.

- 414 [28] M. L. Oyen, R. F. Cook, A practical guide for analysis of nanoindentation data, *Journal of the*
415 *mechanical behavior of biomedical materials* 2 (2009) 396–407.
- 416 [29] B. Preininger, S. Checa, F. L. Molnar, P. Fratzl, G. N. Duda, K. Raum, Spatial-temporal mapping of
417 bone structural and elastic properties in a sheep model following osteotomy, *Ultrasound in medicine*
418 *and biology* 37 (2011) 474–483.
- 419 [30] B. van Rietbergen, J. Kabel, A. Odgaard, R. Huiskes, Determination of trabecular bone tissue elastic
420 properties by comparison of experimental and finite element results, in: *Material identification using*
421 *mixed numerical experimental methods*, Springer, 1997, pp. 183–192.
- 422 [31] H. Daoui, X. Cai, F. Boubenider, P. Laugier, Q. Grimal, Assessment of trabecular bone tissue elasticity
423 with resonant ultrasound spectroscopy, *Journal of the mechanical behavior of biomedical materials* 74
424 (2017) 106–110.
- 425 [32] S. Lakshmanan, A. Bodi, K. Raum, Assessment of anisotropic tissue elasticity of cortical bone from
426 high-resolution, angular acoustic measurements, *IEEE transactions on ultrasonics, ferroelectrics, and*
427 *frequency control* 54 (2007) 1560–1570.
- 428 [33] A. Saïed, K. Raum, I. Leguerney, P. Laugier, Spatial distribution of anisotropic acoustic impedance
429 assessed by time-resolved 50-mhz scanning acoustic microscopy and its relation to porosity in human
430 cortical bone., *Bone* 43 (2008) 187–194. doi:10.1016/j.bone.2008.02.015.
- 431 [34] U. Wolfram, H.-J. Wilke, P. K. Zysset, Transverse isotropic elastic properties of vertebral trabecular
432 bone matrix measured using microindentation under dry conditions (effects of age, gender, and vertebral
433 level), *Journal of Mechanics in Medicine and Biology* 10 (2010) 139–150.
- 434 [35] S. Bernard, Q. Grimal, P. Laugier, Accurate measurement of cortical bone elasticity tensor with resonant
435 ultrasound spectroscopy, *Journal of the mechanical behavior of biomedical materials* 18 (2013) 12–19.
- 436 [36] S. Bernard, J. Schneider, P. Varga, P. Laugier, K. Raum, Q. Grimal, Elasticity-density and
437 viscoelasticity-density relationships at the tibia mid-diaphysis assessed from resonant ultrasound spec-
438 troscopy measurements., *Biomechanics and Modeling in Mechanobiology* 15 (2016) 97–109.
- 439 [37] H. Moulinec, P. Suquet, A numerical method for computing the overall response of nonlinear composites
440 with complex microstructure, *Computer methods in applied mechanics and engineering* 157 (1998) 69–
441 94.
- 442 [38] R. Brenner, Numerical computation of the response of piezoelectric composites using fourier transform,
443 *Physical Review B* 79 (2009) 184106.
- 444 [39] X. Cai, H. Follet, L. Peralta, M. Gardégaront, D. Farlay, R. Gauthier, B. Yu, E. Gineyts, C. Olivier,
445 M. Langer, A. Gourrier, D. Mitton, F. Peyrin, Q. Grimal, P. Laugier, Anisotropic elastic properties of

- 446 human femoral cortical bone and relationships with composition and microstructure in elderly., *Acta*
447 *biomaterialia* (2019). doi:10.1016/j.actbio.2019.03.043.
- 448 [40] H. S. Yoon, J. L. Katz, Ultrasonic wave propagation in human cortical bone - ii. measurements of elastic
449 properties and microhardness, *Journal of biomechanics* 9 (1976) 459–464.
- 450 [41] A. A. E. Orías, J. M. Deuerling, M. D. Landrigan, J. E. Renaud, R. K. Roeder, Anatomic variation in
451 the elastic anisotropy of cortical bone tissue in the human femur, *Journal of the mechanical behavior*
452 *of biomedical materials* 2 (2009) 255–263.
- 453 [42] X. Cai, L. Peralta, P.-J. Gouttenoire, C. Olivier, F. Peyrin, P. Laugier, Q. Grimal, Quantification of
454 stiffness measurement errors in resonant ultrasound spectroscopy of human cortical bone, *The Journal*
455 *of the Acoustical Society of America* 142 (2017) 2755–2765.
- 456 [43] M. Salomé, F. Peyrin, P. Cloetens, C. Odet, A. M. Laval-Jeantet, J. Baruchel, P. Spanne, A synchrotron
457 radiation microtomography system for the analysis of trabecular bone samples, *Medical Physics* 26
458 (1999) 2194–2204.
- 459 [44] T. Weitkamp, P. Tafforeau, E. Boller, P. Cloetens, J.-P. Valade, P. Bernard, F. Peyrin, W. Ludwig,
460 L. Helfen, J. Baruchel, Status and evolution of the esrf beamline id19, in: *X-ray Optics and Microanal-*
461 *ysis: Proceedings of the 20th International Congress*, volume 1221, 2010, pp. 33–38.
- 462 [45] S. Nuzzo, M. Lafage-Proust, E. Martin-Badosa, G. Boivin, T. Thomas, C. Alexandre, F. Peyrin, Syn-
463 chrotron radiation microtomography allows the analysis of three-dimensional microarchitecture and
464 degree of mineralization of human iliac crest biopsy specimens: Effects of etidronate treatment, *Journal*
465 *of Bone and Mineral Research* 17 (2002) 1372–1382.
- 466 [46] J. Schindelin, I. Arganda-Carreras, E. Frise, V. Kaynig, M. Longair, T. Pietzsch, S. Preibisch, C. Rueden,
467 S. Saalfeld, B. Schmid, et al., Fiji: an open-source platform for biological-image analysis, *Nature*
468 *methods* 9 (2012) 676.
- 469 [47] K. Raum, I. Leguerney, F. Chandelier, E. Bossy, M. Talmant, A. Saïed, F. Peyrin, P. Laugier, Bone
470 microstructure and elastic tissue properties are reflected in qus axial transmission measurements, *Ul-*
471 *trasound in medicine & biology* 31 (2005) 1225–1235.
- 472 [48] K. Raum, R. O. Cleveland, F. Peyrin, P. Laugier, Derivation of elastic stiffness from site-matched
473 mineral density and acoustic impedance maps, *Physics in medicine and biology* 51 (2006) 747.
- 474 [49] P. Suquet, *Homogenization Techniques for Composite Media (Lecture notes in Physics, vol. 272)*,
475 Springer-Verlag, 1987, pp. 194–278.

- 476 [50] J. Michel, H. Moulinec, P. Suquet, Effective properties of composite materials with periodic microstructure: a computational approach, *Computer methods in applied mechanics and engineering* 172 (1999)
477 109–143.
478
- 479 [51] J. Swadener, G. Pharr, Indentation of elastically anisotropic half-spaces by cones and parabolae of
480 revolution, *Philosophical Magazine A* 81 (2001) 447–466.
- 481 [52] S. C. Cowin, *Bone mechanics handbook*, CRC press, 2001.
- 482 [53] A. Migliori, J. L. Sarrao, W. M. Visscher, T. M. Bell, M. Lei, Z. Fisk, R. G. Leisure, Resonant ultrasound
483 spectroscopic techniques for measurement of the elastic moduli of solids, *Physica B* 183 (1993) 1 – 24.
484 doi:10.1016/0921-4526(93)90048-B.
- 485 [54] M. Landa, P. Sedlák, H. Seiner, L. Heller, L. Bicanová, P. Šittner, V. Novák, Modal resonant ultrasound
486 spectroscopy for ferroelastics, *Applied Physics A* 96 (2009) 557–567.
- 487 [55] S. Nuzzo, F. Peyrin, P. Cloetens, J. Baruchel, G. Boivin, Quantification of the degree of mineralization
488 of bone in three dimensions using synchrotron radiation microtomography, *Medical physics* 29 (2002)
489 2672–2681.
- 490 [56] J. Y. Rho, P. Zioupos, J. D. Currey, G. M. Pharr, Microstructural elasticity and regional heterogeneity
491 in human femoral bone of various ages examined by nano-indentation, *Journal of biomechanics* 35
492 (2002) 189–198.
- 493 [57] T. Gross, D. H. Pahr, F. Peyrin, P. K. Zysset, Mineral heterogeneity has a minor influence on the
494 apparent elastic properties of human cancellous bone: a *srμct*-based finite element study, *Computer
495 methods in biomechanics and biomedical engineering* 15 (2012) 1137–1144.